

Flow over ice roughness: Part I. Roughness heterogeneity

By X. Hu[†], R. Agrawal, F. Zabaleta, B. Bornhoft, AND X. I. A. Yang[†]

Icing generates surface roughness on lifting surfaces, wherein various roughness statistics vary significantly along the flow direction. This results in the development of non-equilibrium boundary layers. In the present work, we assess and develop equilibrium-type roughness models for boundary layers developing over iced roughnesses in the context of Reynolds-averaged Navier-Stokes (RANS) equations and wall-modeled large-eddy simulations (WMLES). Direct numerical simulations (DNS) are performed, and the resulting DNS data is then used for benchmarking WMLES and RANS. Our *a-posteriori* tests, comparing RANS and WMLES results with benchmark data, demonstrate reasonable agreement. Further, the DNS data also suggests a persisting outer-layer universality, the presence of a logarithmic region, and minimal dispersive stress relative to the Reynolds shear stress. Finally, we also observe the slingshot phenomenon in the Reynolds shear stresses.

1. Introduction

Icing on airfoils can significantly affect both the efficiency and safety of an aircraft. There are two primary types of icing roughness: rime ice and glaze ice (Politovich 2003). Rime ice typically forms under low-temperature conditions, between -10°C and -20°C , and in low-speed environments, where small supercooled water droplets freeze almost instantly upon contact with the airframe. In contrast, glaze ice forms in higher-temperature conditions (0°C to -10°C) and at higher speeds. Larger water droplets do not fully freeze upon contact with the surface, resulting in dense, transparent ice. This process often leads to the formation of horn ice, which significantly alters the aircraft's aerodynamics by increasing drag and reducing lift (Bragg *et al.* 2005). Figure 1 illustrates examples of rime and glaze ice generated experimentally (Broeren *et al.* 2014, 2018). The flow over such ice roughness types includes the interaction of the flow with the rough surface, in addition to the surface curvature, pressure gradients, and ice/flow heterogeneity effects.

Given the high Reynolds numbers typically encountered in these flows, on the order of $Re_c = O(10^6)$ in wind-tunnel tests and higher at real flight conditions, high-fidelity simulations, such as DNS or wall-resolved large-eddy simulations (WRLES), are often computationally prohibitive. Consequently, lower-fidelity approaches, including WMLES and RANS, must be used. However, these involve modeling assumptions that may limit applicability, particularly in post-stall flows or complex ice shapes with significant unsteady effects. In this context, a fundamental study rigorously assessing the underlying modeling assumptions of these methods is lacking. This study aims to fill this gap by offering a detailed evaluation of these models and their effectiveness in predicting aerodynamic degradation due to icing.

In the following, we review the model assumptions in the wall treatments in WMLES and RANS. In WMLES, the equilibrium wall model (EQWM) is the most widely

[†] Department of Mechanical Engineering, the Pennsylvania State University

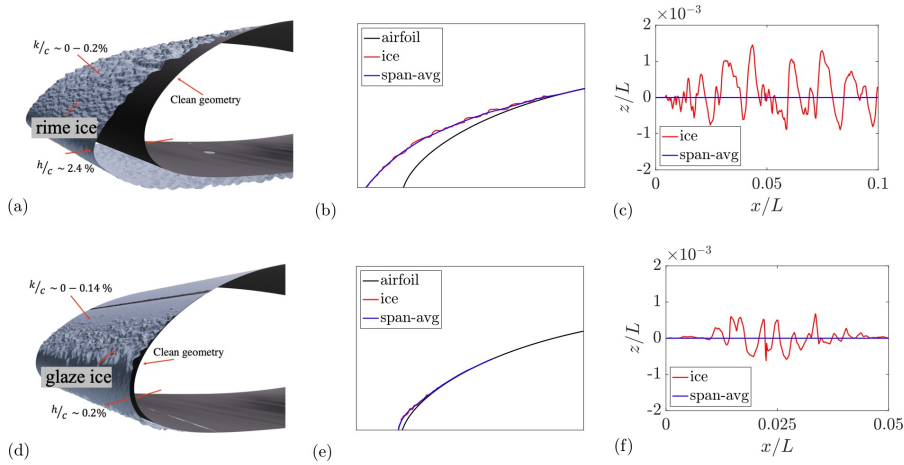


FIGURE 1. (a,d) laser-scanned geometries of icing on NACA23012 airfoil (the exposure time was 5 minutes for the rime ice and 0.5 minute for the glaze ice in the experiment (Broeren *et al.* 2014, 2018); k : roughness length scale; c : clean airfoil chord length; h : displacement height due to ice accretion with respect to the clean geometry); (b,e) sectional cuts of the airfoil; (c,f) unwrapped surface roughness. L is the airfoil chord length. (a,b,c) rime ice; (d,e,f) glaze ice.

used wall treatment (Bose & Park 2018; Larsson *et al.* 2016). This model ignores non-equilibrium effects such as flow acceleration/deceleration and pressure gradients, and it imposes the law of the wall (LoW) between the wall and the LES/wall-model matching location. For rough-wall turbulent boundary layers, the LoW reads

$$U^+ = \frac{1}{\kappa} \ln(z^+) + B - \Delta U^+ = \frac{1}{\kappa} \ln\left(\frac{z}{z_o}\right) = \frac{1}{\kappa} \ln\left(\frac{z}{k_s}\right) + C, \quad (1.1)$$

where z is the wall-normal coordinate, $\kappa \approx 0.38$ is the von Kármán constant, $B \approx 4.3$ is the log-law intercept, ΔU^+ is the roughness function, z_o is the effective roughness height, k_s is the equivalent sand-grain roughness height, and C is a constant that depends on the roughness regime, taking the value of 8.5 in the fully rough regime. Inverting the above scaling provides the following wall treatment,

$$\tau_w / \rho = \left[\frac{\kappa U_{||}}{\ln(h_{wm}/z_o)} \right]^2, \quad (1.2)$$

where h_{wm} indicates the wall-model/LES matching location and $U_{||}$ is the wall-parallel velocity at the matching location. Parameterization of the unresolved surface roughness in terms of k_s , z_o , or ΔU^+ is often not known *a-priori* and must be obtained from laboratory experiments, high-fidelity numerical simulations, or empirical correlation models (Yang *et al.* 2023; Chung *et al.* 2021).

In the RANS context, the classical turbulence models, including Spalart-Allmaras (SA) and k - ω models, have been adapted to include roughness effects. One approach modifies the boundary condition by introducing k_s^+ to account for roughness. For instance, Aupoix & Spalart (2003) extended the SA model to handle rough surfaces by modifying the wall condition and adding an offset to the distance from the wall to account for the roughness height. Similarly, Wilcox (2006) extended the k - ω model to include roughness effects by altering the boundary conditions at the wall. This approach builds on the specific dissipation rate equation for the k - ω model by incorporating surface roughness through a boundary condition that depends on the equivalent sand-grain roughness height, k_s ,

allowing the model to capture the additional drag caused by surface roughness in the fully rough regime without requiring further modification to the turbulence equations. Another strategy for rough-wall RANS modeling is the use of wall functions. These models leverage the shifted log law in rough-wall boundary layers, where the velocity shift is correlated with k_s^+ (Radenac *et al.* 2018; Chedevergne 2018).

In this proceeding, we examine the rough-wall turbulent boundary layer over a flat plate configuration, using an ice roughness geometry obtained from laser scans of iced airfoils (Broeren *et al.* 2014, 2018). In contrast to previous studies, which have typically considered the entire iced airfoil (Bornhoft *et al.* 2024), the present study takes a more fundamental approach, isolating roughness heterogeneity and pressure gradient effects by simulating the developing flow over a flat plate, thus allowing for a clearer evaluation of near-wall model performance. Secondly, we develop equilibrium-type wall models for LES and equilibrium-type wall treatments for RANS. In addition to performing *a-posteriori* tests, where we compare RANS and WMLES results to benchmark DNS data, we directly assess the underlying assumptions of these equilibrium-type models using DNS data. Our findings show that despite the non-equilibrium effects introduced by roughness heterogeneity, the equilibrium-type models provide reasonably accurate predictions of skin friction. We attribute this success to the robustness of the logarithmic region and the LoW.

The remainder of this proceeding is organized as follows. Section 2 provides the computational setup, including the flow configuration in Section 2.1, the roughness geometries in Section 2.2, and the details of DNS, LES, and RANS in Section 2.3. The rough-wall models are discussed in Section 2.5. Section 3 presents the DNS results, while Section 4 evaluates the performance of WMLES and RANS. Finally, concluding remarks are given in Section 5.

2. Computational details

2.1. Flow configuration

Figure 2 presents a schematic of the flow configuration. It consists of a half channel with slip condition on the top boundary, representing the main computational domain, and a concurrent precursor (Stevens *et al.* 2014), which is also a half channel and provides the inflow for the main calculation. Both the precursor and main domains have identical sizes, with dimensions $(L_x, L_y, L_z) = (2\pi\delta, \pi\delta, \delta)$, where x , y , and z denote the streamwise, spanwise, and wall-normal directions, respectively, and δ is the half-channel height. Both domains are periodic in the x and z directions. A fringe region, with a length of $0.125L_x$, is added to the outlet of the main domain to ensure that the flow at the end of the fringe region matches the flow at the end of the precursor domain. In the precursor, the bottom wall is smooth, and the inflow to the main domain is a fully developed half-channel flow. In the main domain, the bottom wall is rough. When the roughness is fully resolved, as in DNS, it is handled using the immersed boundary method (Peskin 2002). In LES and RANS simulations, where the roughness is modeled, a wall model is employed.

2.2. Description of rough walls

Two rough surface types are investigated, corresponding to rime ice and glaze ice. The roughness geometries were obtained by unwrapping laser-scanned experimental icing roughness geometries over the suction side of an airfoil (Broeren *et al.* 2014, 2018) onto a flat plate geometry. The roughness height distributions are shown in Figure 3(a,c).

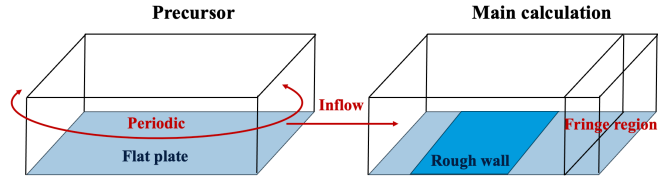


FIGURE 2. A schematic of the flow configuration.

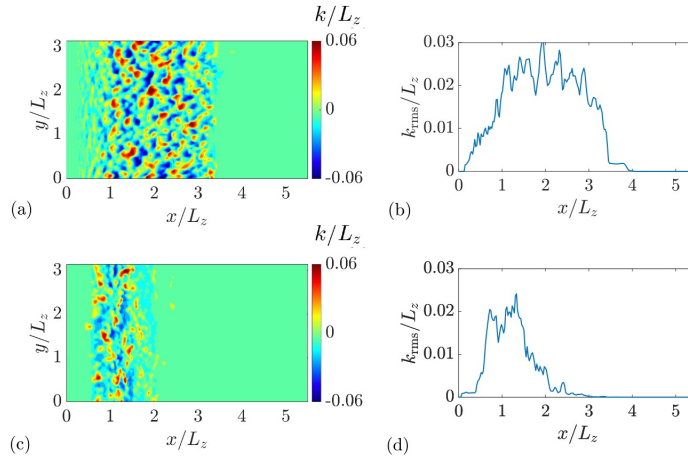


FIGURE 3. (a,c) contours of ice roughness; (b,d) streamwise distribution of the root mean square (rms) of the roughness height. (a,b) rime ice; (c,d) glaze ice.

We scale the roughness such that its trough-to-peak height does not exceed 16% of the half-channel height. This ensures $\delta/k > 6$, and therefore a logarithmic layer can still exist (Flack *et al.* 2007). The k^+ value is close to 70, roughly putting us in the fully rough regime. The rough surfaces are statistically homogeneous in the spanwise direction, y , but heterogeneous in the streamwise direction, x . The mean roughness height, \bar{k} , is zero. Figure 3(b,d) presents the root-mean-square (rms) roughness height distribution, k_{rms} . The rime ice roughness occupies a larger region and has a higher k_{rms} compared to the glaze ice roughness.

2.3. Details of DNS, LES, and RANS

We employ an in-house flow solver, LESGO, for both DNS and LES calculations. This solver utilizes a pseudospectral discretization in the streamwise and spanwise directions, combined with second-order centered finite differences in the wall-normal direction. Time integration is performed using a second-order Adams-Bashforth scheme. The roughness is resolved in DNS but entirely modeled in WMLES. For WMLES, the scale-dependent Lagrangian dynamic model (Bou-Zeid *et al.* 2005) is employed to model the subgrid-scale stress, while the wall model is detailed in Section 2.5. LESGO has been extensively validated for DNS and LES of boundary-layer flows (Yang 2016; Yang & Abkar 2018) and further details of the code can be found in the references.

For the RANS calculations, we use the in-house code GFSI, which is based on a second-order finite volume discretization with Roe's scheme in space and a third-order Runge-Kutta method for time integration. Like WMLES, the entirety of the ice roughness is modeled, and the canopy layer is not resolved. The Prandtl mixing length model is used

to close the Reynolds stress, with a wall treatment detailed in Section 2.5. Like LESGO, GFSI has been thoroughly validated (Luo *et al.* 2022; Zhu *et al.* 2021).

2.4. Case description

The Reynolds number of the flow is $Re_{\tau,0} = \rho u_{\tau,0} \delta / \mu = 395$ at the inlet, where ρ is the fluid density, μ is the dynamic viscosity, u_{τ} is the friction velocity, and δ is the half-channel height. For the DNS simulations, the grid resolution is set to $(N_x, N_y, N_z) = (256, 256, 128)$, yielding a grid resolution of $\Delta_x^+ = 9.7$, $\Delta_y^+ = 4.8$ and $\Delta_z^+ = 3.0$ in the roughness occupied region (note that $\Delta_z^+ = 3$ is sufficient in resolving the surface roughness). For the WMLES simulations, a coarser grid of $(N_x, N_y, N_z) = (32, 32, 12)$ is employed, resulting in a grid resolution of $\Delta_x/\delta = 0.20$, $\Delta_y/\delta = 0.10$, and $\Delta_z/\delta = 0.08$ (note that for WMLES, the grid scales with the local boundary-layer height rather than the viscous length scale). For the RANS simulations, the grid is the same as that of the DNS, ensuring that the resolution is sufficiently fine. A grid convergence study was therefore not conducted. Unlike LES, which converges to DNS with increasing grid resolution (Yang *et al.* 2024), RANS does not approach DNS; instead, it converges to an independent solution which may or may not agree with DNS, depending on the accuracy of the turbulence closure.

2.5. Rough-wall models

For LES, the EQWM in Eq. (1.2) is employed. Considering the roughness heterogeneity, we vary the roughness length scale, z_o , as a function of x . This treatment enables a better representation of both the upstream smooth-to-rough transition and the downstream rough-to-smooth transition. It is important to note that the grid used for WMLES is coarse, with about 13 grid points within the rime ice patch and 5 grid points within the glaze ice patch. Therefore, the variation in z_o reflects the heterogeneity at the scale of the WMLES grid only. Two empirical correlations are used to determine z_o . The first correlation, proposed by Bornhoft *et al.* (2023), can be expressed as

$$\Delta U^+ = c_1 \ln(c_2 k_{\text{rms}}^+ ES) [(c_3 - 1) \tanh(c_4 s_k) + 1] \exp(-c_5 ES^{c_6}), \quad (2.1)$$

where k is the roughness height, k_{rms} is the rms roughness height, ES is the effective slope, s_k is the skewness, $c_1 = 3.026$, $c_2 = 3.444$, $c_3 = 28.56$, $c_4 = 0.0031$, $c_5 = 0.353$, and $c_6 = 0.894$. The second roughness correlation, developed by Flack *et al.* (2020), is given as

$$k_s = c'_1 k_{\text{rms}} (1 + s_k)^{c'_2}, \quad (2.2)$$

where $c'_1 = 3.41$ and $c'_2 = 0.61$. k_s can be related to the roughness length scale z_o as $z_o = k_s \exp(-\kappa C)$, and z_o is related to the roughness function via $z_o^+ = \exp(\kappa(\Delta U^+ - B))$. For the surfaces considered in this work, the roughness parameterization is a function of the streamwise coordinate x , owing to the surface heterogeneity.

In RANS, the unclosed Reynolds shear stress is modeled using the mixing length model

$$R_{13} = l^2 \left(\frac{\partial U}{\partial z} \right)^2, \quad (2.3)$$

where the mixing length l is modeled as

$$\frac{dl}{dz} = \begin{cases} 0 & \text{if } z < k, \\ c & \text{if } z \geq k, \end{cases} \quad (2.4)$$

indicating a constant value in the roughness-occupied layer (Yang & Meneveau 2017; Cionco 1965) and a linear function of the distance from the wall (Prandtl 1925) outside

this layer. Here, c is an unknown constant that must be correlated with ΔU^+ or z_o . The above mixing length model and the velocity profile

$$U^+ = \begin{cases} y/ck & \text{if } z < k, \\ \ln(z/z_o)/\kappa & \text{if } z \geq k, \end{cases} \quad (2.5)$$

together lead to

$$c = \frac{\kappa}{\ln(z/z_o)}. \quad (2.6)$$

Once again, the value of z_o is determined using the same roughness correlations from Bornhoft *et al.* (2023) and Flack *et al.* (2020).

3. DNS results

We present the DNS results, focusing on the aspects that are relevant to rough-wall modeling.

Figure 4 presents the mean flow $\langle u \rangle$, the Reynolds stress $\langle v'v' \rangle$, and the dispersive stress $\langle v''v'' \rangle$ in the streamwise-wall-normal plane, as well as the surface roughness in the streamwise-spanwise plane, for both the rime and glaze ice roughness. The flow fields for the rime ice are shown in Figure 4(a,c,e,g). In Figure 4(a), the roughness patch occupies $x/L_z = 0.5$ to 3.5 . The mean streamwise velocity field, shown in Figure 4(c), reveals that the mean flow is largely parallel, potentially supporting the thin boundary-layer assumption. Figure 4(e) shows the Reynolds stress $\langle v'v' \rangle$. We observe a delayed response to the surface roughness. The roughness enhances the Reynolds stress, but the effect is not strong until $x/L_z \approx 2$ and persists for about one boundary-layer height downstream of the roughness patch. Conversely, the dispersive stress, shown in Figure 4(g), is small compared to its Reynolds stress counterpart and primarily local. This suggests that there are no significant secondary flows extending downstream. The absence of secondary flows aids in maintaining outer-layer similarity (Xu *et al.* 2021; Yang *et al.* 2019), a key hypothesis in rough-wall modeling. The flow fields for the glaze ice are displayed in Figure 4(b,d,f,h). The glaze ice roughness patch is narrower than that of the rime ice, but the results are similar overall. Considering that the flow fields here demonstrate a quick recovery to equilibrium after the roughness patch, with no evidence of long secondary flow structures downstream, we believe the streamwise domain length is appropriate for this case.

Next, we examine the mean streamwise velocity profiles. Figure 5(a,b) shows the mean flow for the rime ice at several x locations. The velocity is normalized using $u_{\tau,0}$, —i.e., the friction velocity at the inlet—in Figure 5(a) and plotted in defect form. Under this normalization, the influence of the roughness is largely confined to the inner layer, while the outer-layer similarity is preserved. In Figure 5(b), we plot U^+ as a function of z^+ using local viscous normalization. The mean velocity profiles at different locations display roughly similar slopes (and a logarithmic layer) but exhibit significantly varying intercepts. Upon encountering the roughness patch, the mean velocity profiles shift downward, consistent with increased skin friction. Similarly, downstream of the roughness patch, the mean velocity profiles gradually return to the equilibrium LoW. The glaze ice results are shown in Figure 5(c,d) and are qualitatively similar to those of the rime ice. However, the glaze ice results show a faster return to equilibrium for the mean velocity profiles in comparison to the rime ice, possibly due to a narrower roughness patch.

We also observe the slingshot effect in the Reynolds shear stress. Figure 6(a,b) presents

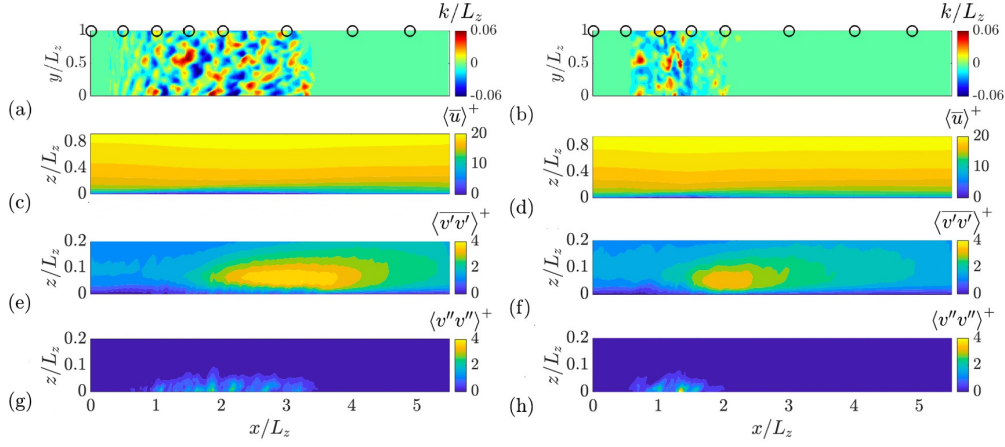


FIGURE 4. (a,b) surface roughness (see Figure 5 for velocity profiles at the circled locations); (c,d) mean streamwise velocity; (e,f) Reynolds stress, $\langle v'v' \rangle$; (g,h) dispersive stress $\langle v''v'' \rangle$. (a,c,e,g) rime ice; (b,d,f,h) glaze ice.

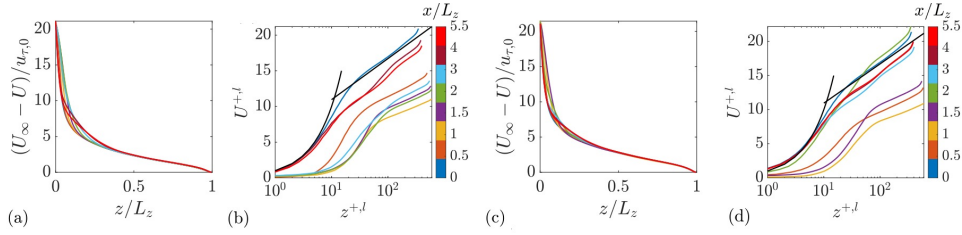


FIGURE 5. Profiles of mean velocity at a number of x locations indicated in Figure 4 (a,b). (a,c) velocity defect; (b,d) mean velocity with local viscous normalization. (a,b) rime ice; (c,d) glaze ice.

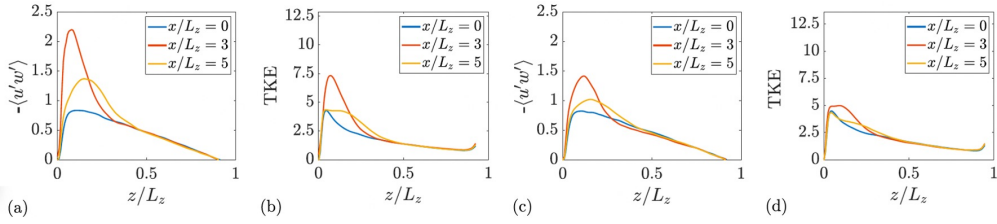


FIGURE 6. (a,c) Reynolds shear stress; (b,d) turbulent kinetic energy. (a,b) rime ice; (c,d) glaze ice.

the Reynolds shear stress and the turbulent kinetic energy (TKE) at three different stations located upstream, within, and downstream of the rime ice roughness patch. Both the Reynolds shear stress and TKE increase as the flow encounters the roughness. However, the Reynolds shear stress response to the surface roughness is disproportionately stronger than that of the TKE. This slingshot effect was first reported in separated flows (Huang 1999). These effects are also observed over glaze ice (see Figure 6(c,d)). We hypothesize that the narrower roughness patch leads to a smaller increase in the Reynolds shear stress as compared to the rime ice.

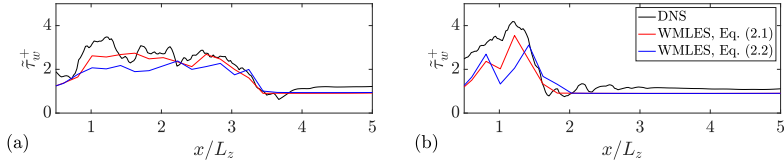


FIGURE 7. The skin friction in WMLES, with normalization by the value at the inlet. (a) rime ice; (b) glaze ice.

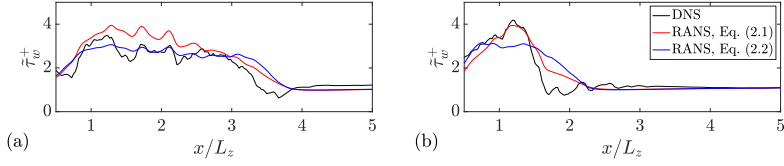


FIGURE 8. The skin friction in RANS, with normalization by the value at the inlet. (a) rime ice; (b) glaze ice.

4. Skin-friction predictions in WMLES and RANS

Finally, we present the WMLES and RANS results and compare them with those of DNS. The discussion is limited to skin friction, which provides a relevant assessment of near-wall turbulence models rather than outer-layer flow quantities (Chen *et al.* 2023; Hansen *et al.* 2023). The RANS and WMLES results should be viewed as predictive, given that the roughness correlations were not specifically trained for the ice roughness in this configuration. Furthermore, equilibrium-type models are applied to non-equilibrium flows in this case.

Figure 7 presents WMLES results. For the rime ice, the variation of skin friction is well captured by the WMLES. The correlation given by Eq. (2.1) is slightly more accurate than the one in Eq. (2.2). For the glaze ice, the higher skin friction is concentrated over a narrower streamwise extent than with DNS. Some discrepancies are observed during the smooth-to-rough transition, but the overall agreement remains reasonable, especially given the coarse resolutions. Similar to that in the rime ice case, Eq. (2.1) provides slightly better prediction of the sharp rise in skin friction at $x/L_z \approx 1$ compared to Eq. (2.2).

Figure 8 provides the RANS results. In comparison to WMLES, the RANS results are in better agreement with the DNS results for both ice cases. For the rime ice, the correlation in Eq. (2.2) provides slightly more accurate results than Eq. (2.1), whereas the opposite is true for the glaze ice. We emphasize that the RANS mesh is finer than the WMLES, allowing RANS to capture some of the smaller variations in skin friction.

5. Conclusions

In this proceeding, we investigated the flow over ice roughness using DNS, WMLES, and RANS approaches. The roughness geometries were unwrapped from laser-scanned icing surfaces, allowing us to focus on the effect of roughness heterogeneity in the streamwise direction. Our DNS revealed that for these surfaces, the roughness significantly impacts the inner layer, while the outer-layer similarity and the log layer are preserved, thereby potentially supporting local turbulence parameterization. Both rime and glaze ice geometries induced a pronounced slingshot effect in the Reynolds shear stress.

We developed and tested new near-wall treatments for both RANS and WMLES,

incorporating roughness effects via empirical correlations. These models were compared against DNS data and demonstrated reasonable accuracy in predicting skin friction for both rime and glaze ice. WMLES captured the variations in skin friction over the rough surfaces well, despite its coarse streamwise grid, while RANS, with its finer streamwise grid, was able to resolve more detailed flow features. A second part of the work will be presented in the 2024 Center for Turbulence Research Annual Research Briefs, focusing on pressure gradient and heat transfer and providing additional details for near-wall modeling.

Acknowledgments

Yang and Hu thank the participants of the fundamentals group at the 2024 CTR summer program. Zhongxin Yang and Wen Zhang are acknowledged for their generous help.

REFERENCES

- AUPOIX, B. & SPALART, P. 2003 Extensions of the Spalart–Allmaras turbulence model to account for wall roughness. *Int. J. Heat Fluid Flow* **24**, 454–462.
- BORNHOFT, B., JAIN, S. S., GOC, K., BOSE, S. T. & MOIN, P. 2024 Large-eddy simulations of the NACA23012 airfoil with laser-scanned ice shapes. *Aerosp. Sci. Technol.* **146**, 108957.
- BORNHOFT, B., JAIN, S. S. & MOIN, P. 2023 A velocity transformation for rough-wall-bounded turbulent flows. *Annual Research Briefs*, Center for Turbulence Research, Stanford University. pp. 293–305.
- BOSE, S. T. & PARK, G. I. 2018 Wall-modeled large-eddy simulation for complex turbulent flows. *Annu. Rev. Fluid Mech.* **50**, 535–561.
- BOU-ZEID, E., MENEVEAU, C. & PARLANGE, M. 2005 A scale-dependent Lagrangian dynamic model for large eddy simulation of complex turbulent flows. *Phys. Fluids* **17**, 025105.
- BRAGG, M., BROEREN, A. & BLUMENTHAL, L. 2005 Iced-airfoil aerodynamics. *Prog. Aerosp. Sci.* **41**, 323–362.
- BROEREN, A. P., ADDY, H. E., LEE, S. & MONASTERO, M. C. 2014 Validation of 3D ice accretion measurement methodology for experimental aerodynamic simulation. *AIAA Paper* 2014-2614 .
- BROEREN, A. P., JR., H. E. A., LEE, S., MONASTERO, M. C. & MCCLAIN, S. T. 2018 Three-dimensional ice-accretion measurement methodology for experimental aerodynamic simulation. *J. Aircraft* **55**, 817–828.
- CHEDEVERGNE, F. 2018 Analytical wall function including roughness corrections. *Int. J. Heat Fluid Flow* **73**, 258–269.
- CHEN, P. E., WU, W., GRIFFIN, K. P., SHI, Y. & YANG, X. I. A. 2023 A universal velocity transformation for boundary layers with pressure gradients. *J. Fluid Mech.* **970**, A3.
- CHUNG, D., HUTCHINS, N., SCHULTZ, M. P. & FLACK, K. A. 2021 Predicting the drag of rough surfaces. *Ann. Rev. Fluid Mech.* **53**, 439–471.
- CIONCO, R. M. 1965 A mathematical model for air flow in a vegetative canopy. *J. Appl. Meteor.* **4**, 517–522.
- FLACK, K., SCHULTZ, M. & BARROS, J. 2020 Skin friction measurements of

- systematically-varied roughness: probing the role of roughness amplitude and skewness. *Flow Turbul. Combust.* **104**, 317–329.
- FLACK, K. A., SCHULTZ, M. P. & CONNELLY, J. S. 2007 Examination of a critical roughness height for outer layer similarity. *Phys. Fluids* **19**, 095104.
- HANSEN, C., YANG, X. I. A. & ABKAR, M. 2023 A POD-mode-augmented wall model and its applications to flows at non-equilibrium conditions. *J. Fluid Mech.* **975**, A24.
- HUANG, P. G. 1999 Physics and computations of flows with adverse pressure gradients. In *Salas, M.D., Hefner, J.N. & Sakell, L. (eds) Modeling Complex Turbulent Flows* (pp.245-258). Springer.
- LARSSON, J., KAWAI, S., BODART, J. & BERMEJO-MORENO, I. 2016 Large eddy simulation with modeled wall-stress: recent progress and future directions. *Mech. Eng. Rev.* **3**, 15–00418.
- LUO, F., GAO, C. & ZHANG, W. 2022 The key to suppress vortex-induced vibration: stability of the structural mode. *J. Fluid. Struct.* **113**, 103692.
- PESKIN, C. S. 2002 The immersed boundary method. *Acta Numer.* **11**, 479–517.
- POLITOVICH, M. K. 2003 Aircraft icing. In *Curry, J. A. & Pyle, J. A. (eds.), Encyclopedia of Atmospheric Sciences* (pp.68-75). Academic Press.
- PRANDTL, L. 1925 Bericht uber untersuchungen zur ausgebildeten turbulenz. *Z. Angew. Math. Mech.* **5**, 136–139.
- RADENAC, E., KONTOGIANNIS, A., BAYEUX, C. & VILLEDIEU, P. 2018 An extended rough-wall model for an integral boundary layer model intended for ice accretion calculations. *AIAA Paper* 2018-2858 .
- STEVENS, R. J. A. M., GRAHAM, J. & MENEVEAU, C. 2014 A concurrent precursor inflow method for large eddy simulations and applications to finite length wind farms. *Renew. Energ.* **68**, 46–50.
- WILCOX, D. C. 2006 Turbulence modeling for CFD. DCW industries .
- XU, H. H., ALTLAND, S. J., YANG, X. I. A. & KUNZ, R. F. 2021 Flow over closely packed cubical roughness. *J. Fluid Mech.* **920**, A37.
- YANG, X. I. A. 2016 On the mean flow behaviour in the presence of regional-scale surface roughness heterogeneity. *Bound.-Lay. Meteorol.* **161**, 127–143.
- YANG, X. I. A. & ABKAR, M. 2018 A hierarchical random additive model for passive scalars in wall-bounded flows at high Reynolds numbers. *J. Fluid Mech.* **842**, 354–380.
- YANG, X. I. A., ABKAR, M. & PARK, G. I. 2024 Grid convergence properties of wall-modeled large eddy simulations in the asymptotic regime. *J. Fluid. Eng.* **146**, 081501.
- YANG, X. I. A. & MENEVEAU, C. 2017 Modelling turbulent boundary layer flow over fractal-like multiscale terrain using large-eddy simulations and analytical tools. *Philos. T. Roy. Soc. A.* **375**, 20160098.
- YANG, X. I. A., XU, H. H. A., HUANG, X. L. D. & GE, M. W. 2019 Drag forces on sparsely packed cube arrays. *J. Fluid Mech.* **880**, 992–1019.
- YANG, X. I. A., ZHANG, W., YUAN, J. & KUNZ, R. F. 2023 In search of a universal rough wall model. *J. Fluid. Eng.* **145**, 101302.
- ZHU, L., ZHANG, W., SUN, X., LIU, Y. & YUAN, X. 2021 Turbulence closure for high Reynolds number airfoil flows by deep neural networks. *Aerosp. Sci. Technol.* **110**, 106452.